Estimation of Personalized Minimal Purkinje Systems From Human Electro-Anatomical Maps

Fernando Barber, Peter Langfield, Miguel Lozano, Ignacio García-Fernández, Josselin Duchateau, Mélèze Hocini, Michel Haïssaguerre, Edward Vigmond, and Rafael Sebastian

***Abstract*— The Purkinje system is a heart structure responsible for transmitting electrical impulses through the ventricles in a fast and coordinated way to trigger mechanical contraction. Estimating a patient-specific compatible Purkinje Network from an electro-anatomical map is a challenging task, that could help to improve models for electrophysiology simulations or provide aid in therapy planning, such as radiofrequency ablation. In this study, we present a methodology to inversely estimate a Purkinje network from a patient's electro-anatomical map. First, we carry out a simulation study to assess the accuracy of the method for different synthetic Purkinje network morphologies and myocardial junction densities. Second, we estimate the Purkinje network from a set of 28 electro-anatomical maps from patients, obtaining an optimal conduction velocity in the Purkinje network of 1.95 ± 0.25 m/s, together with the location of their Purkinje-myocardial junctions, and Purkinje network structure. Our results showed an average local activation time error of 6.8 ± 2.2 ms in the endocardium. Finally, using the personalized Purkinje network, we obtained correlations higher than 0.85 between simulated and clinical 12-lead ECGs.**

***Index Terms*— Purkinje system, electro-anatomical maps, personalized electrical activation, arrhythmia.**

Manuscript received March 15, 2021; accepted April 11, 2021. Date of publication April 15, 2021; date of current version July 30, 2021. This work was supported in part by the "Programa Estatal de Investigacion, Desarrollo e Innovacion Orientado a los Retos de la Sociedad" from the Ministerio de Economia y Competitividad of Spain, Agencia Estatal de Investigacion, and the European Commission (European Regional Development Funds-ERDF-FEDER) under Award TIN2014-59932-JIN, in part by the Leducq Foundation under Grant 16 CVD 02 and GENCI computing resources, allocation under Grant A0080310517, and in part by the French Government as part of the "Investments of the Future" program managed by the National Research Agency (ANR), under Grant ANR-10-IAHU-04. *(Corresponding author: Rafael Sebastian.)*

This work involved human subjects or animals in its research. Approval of all ethical and experimental procedures and protocols was granted by Bordeaux University Hospital (CHU) and performed in line with GDPR and the Helsinki Convention.

Fernando Barber, Miguel Lozano, Ignacio García-Fernández, and Rafael Sebastian are with the Computational Multiscale Simulation Laboratory (CoMMLab), Department d'Informàtica, Universitat de València, 46100 Valencia, Spain (e-mail: rafael.sebastian@uv.es).

Peter Langfield and Edward Vigmond are with IHU Liryc, Electrophysiology and Heart Modeling Institute, Fondation Bordeaux Université, 33600 Bordeaux, France, and also with the Institut de Mathématiques de Bordeaux (IMB), UMR 5251, University of Bordeaux, 33400 Talence, France.

Josselin Duchateau, Mélèze Hocini, and Michel Haïssaguerre are with IHU Liryc, Electrophysiology and Heart Modeling Institute, Fondation Bordeaux Université, 33600 Bordeaux, France, and also with the Cardiac Electrophysiology and Cardiac Stimulation Team, Bordeaux University Hospital (CHU), 33000 Bordeaux, France.

Digital Object Identifier 10.1109/TMI.2021.3073499

I. Introduction

THE Purkinje system (PKN) is a network responsible for the fast transmission of the electrical impulses that trigger the ventricular depolarization [1]. In human hearts, the network extends over the right (RV) and left ventricular (LV) endocardium as well as within the trabeculae carnae, allowing a faster and more synchronized activation of the myocardium, and an efficient contraction [2]. From a geometrical point of view, it can be seen as a set of interconnected 1D cables, that branch and anastomose, connecting to the underlying endocardial tissue at discrete locations, known as Purkinje-myocardial junctions (PMJs). The fascicular structures are so thin that can not be differentiated in-vivo with clinical imaging acquisition techniques such as magnetic resonance imaging (MRI) or computed tomography (CT). Therefore, the characterization or reconstruction of the PKN from patient-specific human data is a challenging problem [3]. In humans, high-resolution imaging techniques have allowed only the segmentation of proximal sections of the PKN from images acquired ex vivo in combination with specific markers [4], [5]. In animals, several studies have analyzed and modelled either the proximal sections macroscopically [6], [7], or random sections observed with the combination of confocal microscopy and specific inks [8].

An alternative way to reconstruct the PKN is to estimate it inversely from electrical activation sequences from the endocardium by means of electro-anatomical maps (EAMs). EAMs can be acquired in vivo, using catheters that map the electrical activity of a patient in real-time, producing a spatio-temporal map of the activation sequence (LAT). Therefore, the structure can be estimated not from images but from the electrical sequence that produces when it activates.

Some methods have already been presented to estimate the PKN from EAMs, by building an initial random fractal network, and reducing the activation time error by moving, adding or pruning branches and PMJs from the initial network [9] or looking for local minima on EAMs and placing there PMJs [10].

Clinically, the PKN structure is very relevant since it is responsible for the initiation and maintenance of certain life-threatening arrhythmias. For instance, it is known that some His-Purkinje system-related macro re-entry ventricular tachycardias (VT) are triggered or supported by the PKN, and that the ablation of specific Purkinje-myocardial

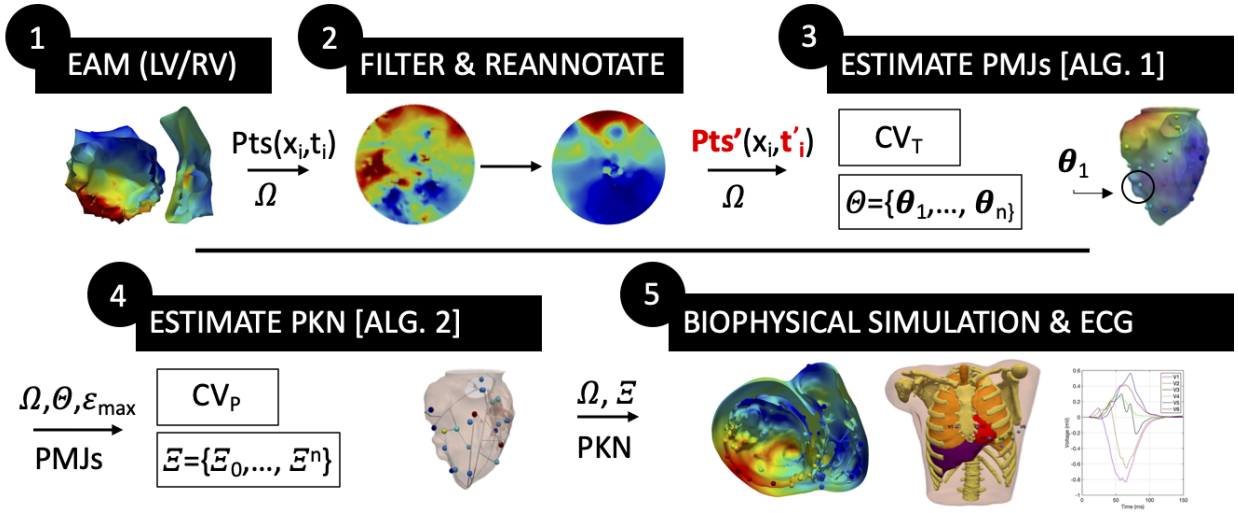

Fig. 1. Pipeline designed to estimate a PKN from an EAM and carry out personalized electrical simulations. Arrows before each step indicate the input parameters required from previous steps or the user. Pts is the list of sampled points in the EAM, Pts' are the points filtered and re-annotated, Ω stands for the anatomical domain (endocardium), Θ is the list of PMJs, Ξ is the list of branches and connected PMJs, and ϵ_{max} is the maximum error allowed to connect a PMJ to Ξ. CV_T and CV_P stands for the estimated conduction velocity for tissue and Purkinje, respectively.

junctions (PMJs) or bundles can stop the arrhythmia [11]. Radio-frequency ablation (RFA) is considered a potential first-line therapy for patients with idiopathic VT, because these VTs can be eliminated by ablation in a high percentage of patients. However, in some types such as focal Purkinje VT, the recurrence rate is around 29% [12], and there are several complications associated with ablation. In cases of idiopathic ventricular fibrillation (IVF), the main cause of unexplained sudden cardiac death, the majority of cases (up to 93%) are triggered by premature ventricular contractions (PVCs) that originate from the PKN [13]. Finally, it is important to add that some patient might develop symptoms to some pathologies such as heart failure when in sinus rhythm, which makes also very important to understand the His-Purkinje system with more detail.

All these facts evidence the necessity of being able to incorporate a PKN in personalized biophysical heart models aimed to simulate and reproduce several types of arrhythmia. However, the construction of a realistic computational PKN for humans is complex, and in general does not provide a personalized activation sequence [7]. Therefore, generic PKN models are usually included in 3D ventricles for mechanistic studies [3].

In this paper, we present a pipeline (see Fig. 1) to first estimate the location of a set of PMJs from EAMs based on an improved version of the algorithm presented in [14], and second, one of the main contributions of this study, an algorithm to estimate a simplified PKN from the EAM, based on the location and activation time of the PMJs. The pipeline has been validated on several synthetic PKN configurations, with simulated activation maps, subject to different activation time error amplitudes, where we assess geometrical and electrical differences in estimated PKN. Following, the algorithm has also been tested on a set of 28 clinical datasets (14 LV and 14 RV EAMs) obtained from patients in sinus rhythm without structural heart disease. As a result, we obtained for every case, the PKN model, the optimal conduction velocity (CV) in the PKN, and an average LAT error from direct comparison of simulated and patient clinical data. The simulated activation sequence using the estimated PKN together with estimated CVs for tissue and Purkinje, provided a good match between simulated and clinical 12-lead ECGs, validating the PKN sequence of activation. To our knowledge this is the largest validation of such estimation methods carried using clinical data.

TABLE I
SUMMARY OF FIVE SYNTHETIC PKNS

Scenario				TAT (ms)	
Name	# PMJ	# PMJ/Seg	# Br	PKN	ENDO
PK1	1224	76.5 ± 0.7	2650	56.3	78.3
PK2	831	51.9 ± 1.1	1908	78.2	110.4
PK3	442	27.6 ± 0.6	948	64.2	86.5
PK4	362	22.6 ± 0.7	830	63.5	86.1
PK5	206	14.7 ± 0.6	298	67.7	89.7

II. MATERIAL AND METHODS

A. Synthetic Models

We built a set of five synthetic PKNs on a generic LV endocardium, reconstructed from a MRI sequence, using the stochastic method described in [7]. The properties of the PKNs are summarized in Table I. Column *Name* identifies the scenario, *PMJ* represents the number of PMJs in the scenario, *Density* is the average and standard deviation of the number of PMJs per segment (17 AHA segment division), *TAT PKN* is the total activation time of the Purkinje Network, *TAT ENDO* is the total activation time for the whole endocardium.

First, we will evaluate the performance of the PKN estimation, by using all the PMJs from the original model and without measurement error ($\sigma = 0$), and compare estimated and original PKNs. Following, we will develop more complex scenarios in which for each original PKN we: i) simulate the

corresponding His-Purkinje LAT map for the endocardium; ii) sample the activation times on the endocardial tissue randomly at a number of locations (1000 samples), mimicking a virtual EAM; iii) we add Gaussian noise to the LAT values to emulate measurement errors, or wrongly annotated samples; iv) we estimate the PMJs from the noisy samples; and v) we estimate the PKN associated to these estimated PMJs. Note that since all PMJ LATs are relative to the activation of the atrio-ventricular node, i.e., the first node of the PKN, and that we only consider anterograde activation (from PKN to tissue) we have not added the PMJ delays, which will imply adding a fix and constant delay to all the PMJs.

B. Patient Data

A total of 28 EAM datasets (from 13 patients, where P13 was mapped twice) have been included in the study. Anonymized EAMs (12 men and 1 women, between 16 and 63 years old) were provided by Bordeaux University Hospital using CARTO 3 system (Biosense Webster, Inc., Diamond Bar, CA, USA), and different catheters namely, NaviStar ThermoCool ablation catheter and PentAray (see Table III Patient columns, where 'A/S' stands for age and sex, and 'Ind' stands for the clinical indication). The patients had an indication of either idiopathic VF (IVF) or syncope, hypertrophic cardiomyopathy (HCM), Brugada Syndrome (BS) or ventricular tachycardia (VT). For two patients, P12 and P13, MRI data was also available. For every patient, three studies were acquired in sinus rhythm: a map of the LV endocardium, a map of the RV endocardium and a map of the epicardium (not used or required in this study). Five patients benefited from high density endocardial mapping with a decapolar catheter to map the endocardium of the RV and LV (P1, P2, P6, P8, P9).

For each EAM, the set of measurement points was filtered to ensure the quality of the data. In particular, points exhibiting non physiological peak-to-peak amplitudes or LAT values were disregarded (see Table III Sampl. column (acquired samples) vs. #Pts (samples kept)). In particular, sample points with a bipolar peak-to-peak amplitude below 1.5 mV or with a local activation time outside the range $[-200, 200]$ ms, or farther than 7 mm away from the endocardial wall were discarded. After this filtering, LAT annotations of the EAMs were automatically determined by the Confidense module of CARTO 3 System. However, large delays between close areas, where there was no underlying substrate that could explain them, were observed in most patients due to wrong time annotations at sample points. We re-annotated each EAM sample using a tailor-made Matlab code that selects the deflection on the distal bipolar signal (M1-M2) closest to the point of maximum negative slope on the distal unipolar signal (M1).

Fig. 2 (second row) presents the resulting LV EAMs in 5 patients after the data was filtered and re-annotated. After the re-annotation of the samples, a linear interpolation was performed to obtain the LAT on every point of the 3D mesh.

For visualization purposes, in this study the LAT maps are projected into a unitary 2D disk using a quasi-conformal projection (QCM) as in [15]. In particular, we used the conformal energy minimization (CEM) algorithm [16], based on discrete Laplace-Beltrami operator. It is important to point out that this transformation on a ventricular geometry does not respect distances and produces a compression of the points that are in the apical area, and an expansion of the points in the basal area. However, this representation is very convenient to compare data from different LV geometries in a common reference space. To avoid inconsistencies, the trabeculations that crosses the ventricular cavity, and the papillary muscles were removed to obtain a smooth surface without holes before the projection was performed.

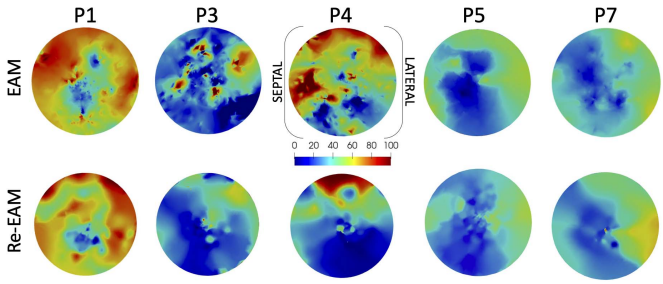

Fig. 2. LV original EAMs and re-annotated EAM, projected into a 2D unitary disk. A set of 5 EAMs, as they are obtained from the system (top row), and after applying filters, and re-annotating the local activation maps (bottom row). After the re-annotation, the data was linearly interpolated on the 3D mesh, and projected using a quasi-conformal transformation onto a disk. The colorbar describes the local activation time from blue ($t = 0$ms), to red ($t = 100$ms).

C. Algorithm for PMJ Estimation

To estimate a set of PMJ, we use the method proposed by Barber *et al.* in [14], which is briefly described here. The interested reader can find a detailed description of the algorithm therein. In this PMJ estimation method, the endocardial domain is discretized by means of an homogeneous simplicial 2-complex in a three-dimensional space, $\mathbf{\Omega}$. The EAM, either synthetic or acquired during an intervention, is defined by a set $\mathcal{P}$ of measurement points. All these points belong to the set $\mathcal{V}$ of the vertices of $\mathbf{\Omega}$. The procedure takes the location $\mathbf{p}_i$ and LAT t_i of the points in $\mathcal{P}$, to generate a set of points $\Theta \subseteq \mathcal{V}$ that are compatible with the observed activation times. The set $\mathcal{V}$ is traversed to evaluate if each vertex is a feasible activation point. By means of a hypothesis contrast, if a given vertex can be considered a PMJ, then a new candidate θ_i is added to Θ. This step is done in lines 1–8 of Algorithm 1. After the generation of the set Θ of candidate PMJs, all the $\theta_i \in \Theta$ are evaluated to determine their quality. Since the activation of the points in $\mathcal{P}$ is a consequence of the activation of the PMJ, we test whether the points activated by the candidates θ_i with higher activation time can also be explained by PMJ that activated earlier. If that is the case, the oldest PMJ are removed. This is described in lines 10–18 of Algorithm 1.

One of the key steps of the algorithm is the assessment of the activation times τ_i (line 3 of Algorithm 1. As described in [14], this is done using a characterization of the PMJ that considers the heart activation as a deterministic process subject to random measurement error. Under this assumption,

Algorithm 1 Estimation of PMJs From EAMs

1: **for all** $\mathbf{x} \in \mathcal{V}$
2: $\quad \mathcal{T} \leftarrow \{\tau_i(\mathbf{x}) = t_i - d(\mathbf{p}_i, \mathbf{x})/\upsilon, \quad : (\mathbf{p}_i, t_i) \in \mathcal{P}\}$
3: $\quad \mathcal{T}_{ok} \leftarrow \{\tau_i \in \mathcal{T} :$ is a compatible activation time$\}$
4: $\quad$ **if** $|\mathcal{T}_{ok}| \geq 3$,
5: $\quad\quad$ Add ($\mathbf{x}$, $\mathcal{T}_{ok}$) to Θ
6: $\quad\quad A(\mathbf{x}) \leftarrow \{\mathbf{p}_i : \mathbf{p}_i$ can have been activated by $\mathbf{x}\}$
7: $\quad$ **end if**
8: **end for**
9: $\Theta \leftarrow sort(\Theta, key = \tau_i, decreasing)$
10: **repeat**
11: $\quad changed \leftarrow False$
12: $\quad$ **for all** $\theta \in \Theta$
13: $\quad\quad$ **if** $\forall\ \mathbf{p}\ \in A(\theta), \exists\ \theta' \neq \theta \in \Theta : \mathbf{p}\ \in A(\theta')$,
14: $\quad\quad\quad \Theta \leftarrow \Theta - \{\mathbf{x}\}$
15: $\quad\quad\quad changed \leftarrow True$
16: $\quad\quad$ **end if**
17: $\quad$ **end for**
18: **until** $not(changed)$
19: **Output** $\leftarrow \Theta$

the values of the τ_i for a given candidate PMJ are tested by means of a hypothesis contrast. In order to make this step more robust, we have introduced an additional condition before accepting a set of activation times as a compatible set. We note that there must be a linear relationship between the activation times of the compatible measurement points t_i and the distances $d(\mathbf{p}_i, \mathbf{x})$. The introduction of this additional requirement to build $\mathcal{T}_{ok}$ in line 3 of the algorithm reduces the size of Θ by around a 10% preventing the inclusion of spurious PMJ and, subsequently, saving time in the second part of the algorithm.

The set of PMJs is estimated for a range of predefined tissue conduction velocities (CVs), from 0.4 to 0.9 m/s, to take into account potential slow propagation due to pathological tissue such as fibrosis, among others. Finally, after testing all the CVs, the estimated set of PMJs with less average error at the sampling points, Δ_{EAM}, is the one kept for the next stage. Note that, although fiber orientation is considered in the forward propagation, for the estimation of PMJs we used geodesic distances on the endocardial surface, which does not use the underlying fiber orientation. In that sense, it is important to point out that the extensive trabecullations observed in the inner surface of the ventricles [17] do not follow the fiber orientation (described for the subendocardial area (∼60 degrees) [18]), but one defined by the main direction of the trabecullae), and the PKN is thought to run inside them.

D. Algorithm for PKN Estimation

The proposed method starts with the estimation of the PMJs from an EAM (see Fig. 1, step 3), as described in previous section. The ultimate goal of the PKNs estimation algorithm is to find a PKN branching configuration that is able to connect all the estimated PMJs at the estimated LATs, with the minimum number of branches and error (see Fig. 1, step 4). We start by considering the set of estimated PMJs that were

Algorithm 2 Estimation of PKN for a Set of Given PMJs

1: $ListBranches \leftarrow \Xi^0$
2: **for all** $\epsilon \in [1, \epsilon_{max}]$
3: $\quad$ **for all** $\theta_i \in \Theta$
4: $\quad\quad (\mathbf{x}_i, t_i) \leftarrow \theta_i$
5: $\quad\quad [\xi_i] \leftarrow \text{argmin}_{\xi_i \in \Xi^{i-1}} \left\{ t_i - \left(t(\xi_i) + \frac{|\xi_i - \mathbf{x}_i|_\Omega}{\upsilon} \right) \right\}$
6: $\quad\quad$ **if** $(\xi_i \leq \epsilon)$ and $\Xi^{i-1} \cap$ ListBranches $= \emptyset$
7: $\quad\quad\quad$ Add Ξ^{i-1} to $listBranches$
8: $\quad\quad\quad$ Remove θ_i from Θ
9: $\quad\quad$ **end if**
10: $\quad$ **end for**
11: **end for**
12: **Output** $\leftarrow listBranches$

obtained in the previous step, $\Theta = \{\theta_1, \ldots, \theta_n\} \subset \mathcal{V} \times \mathcal{R}^+$. For each PMJ $\theta_i = (\mathbf{x}_i, t_i)$, the point $\mathbf{x}_i \in \Omega$ (nodes on the endocardial surface) will be called the location and $t_i \in \mathcal{R}^+$ the estimated LAT at the PMJ. Without loss of generality, we will assume that PMJs are in ascending order of LAT, that is, $i \leq j \Rightarrow t_i \leq t_j$. We will also consider, Ξ, a connected simplicial 1-complex to represent the branches that form the PKN. Each vertex or node in Ξ will have an associated LAT, that corresponds to its activation time according to the PKN generated and the CV_P through the PKN. The estimated PKN, will have the constraint that all the vertices of Ξ will be in a vertex or an edge of Ω, and all the edges of Ξ will coincide with an edge of Ω or will be contained in one of its faces. Moreover, the terminal vertices of Ξ have to be locations of the estimated PMJs.

We build the estimated PKN in an iterative fashion (see Algorithm 2). An initial branch Ξ^0, corresponding to the His bundle and left bundle branch (LBB), is built before the algorithm generates any further branch. The initial branch always starts from a location determined by the user and expands to the apex through the septal wall following the shortest path, which is obtained by calculating the geodesic path between both points. Then, we process the PMJs in order of LAT, starting by the earliest one. Therefore, we start building the PKN from the region closer to the LBB, which is expected to show smaller LAT errors due to the shorter path from the Atrioventricular Node (AVN).

After step i, we have processed $i-1$ PMJs in Θ and have built an estimated tree Ξ^{i-1} that connects them. We pick θ_i and solve the fast marching method on Ω starting from θ_i to obtain the distance from the estimated PMJ to all the vertices on Ξ^{i-1}. Then, we try to connect the PMJ θ_i with Ξ^i using a geodesic that ends at a point $\xi_i \in \Xi^{i-1}$. The connection point is chosen as the solution of the optimization problem

$$\xi_i = \text{argmin}_{\xi_i \in \Xi^{i-1}} \left\{ t_i - \left(t(\xi_i) + \frac{|\xi_i - \mathbf{x}_i|_\Omega}{\upsilon} \right) \right\}, \quad (1)$$

$$s.t. \quad \text{path}_\Omega(\xi_i, \mathbf{x}_i) \cap \Xi^{i-1} = \emptyset, \quad (2)$$

where $|\cdot|_\Omega$ is the geodesic distance on Ω, $\text{path}_\Omega(\xi_i, \mathbf{x}_i)$ is the geodesic created to connect $\mathbf{x}_i$ with ξ_i, and υ is the CV_P in the PKN. With the constraint on the path, we exclude new branches that intersect the PKN created so far. In summary,

we are trying to connect the estimated PMJ to the current PKN at a location so that the LAT at the PMJ matches the estimated one, provided a CV_P, υ, inside the PKN. Only solutions with an error value, $\Delta_{PMJ} < \epsilon_n$ (user-defined threshold at iteration n), will generate a new branch for the PKN in each iteration. In cases in which the residual in Eq. 1 is above the threshold, the candidate θ_i is not connected. Once the iteration ends with the last θ_i, the process is restarted trying to connect the disregarded PMJs to the estimated PKN, using a larger threshold. The algorithm stops when all the PMJs have been connected to Ξ or when the error threshold in the unconnected PMJs reaches a predefined bound (ϵ_{max}).

After each iteration, the set of remaining PMJs can only be reduced or, in the worst case, remain without changes. As a result, the algorithm is guaranteed to stop either by the integration of all the PMJs in the PKN or by the removal of all the remaining PMJs when ϵ_{max} is reached. The PKN built by means of Algorithm 2 it is not the unique possible PKN compatible with the observed EAM. It has, however, the property of being *minimal* in the sense that it is formed by geodesic curves in Ω.

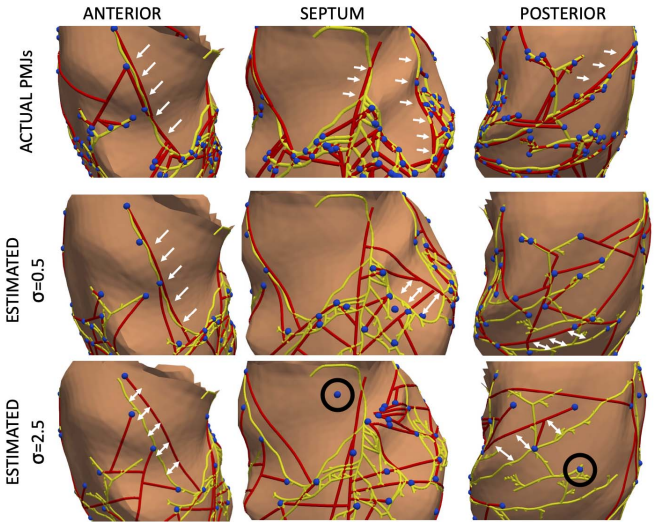

Fig. 3. Detailed comparison of PK3 with different Gaussian noise in the samples. PKNs are rendered with tubes, yellow for the original, and red for the estimated. Blue spheres are the PMJs, either original or estimated (for Gaussian noise $\sigma = 0.5$ and $\sigma = 2.5$). Single headed white arrows point out a perfect fit between original and estimated PKN, while double headed arrows show the displacement between them. Black circles point out PMJs not connected to the tree due to temporal errors.

III. Results

A. Estimation of PKN From Synthetic Models

For the five synthetic PK scenarios, we obtained the set of estimated PMJs, and the set of estimated PKNs. For the estimation of PKNs, we compared the results when using as an input to the algorithm either original PMJs (Table II, $\sigma = 0$) or estimated PMJs (Table II, $\sigma = [0.5; 2.5]$).

As it can be observed, when using the original PMJs (location and LAT taken directly from the model) the errors, Δ_{PMJs} and Δ_{EAM}, are smaller, and the PKN structure is reproduced more accurately, i.e, the distance between the original PKN and the estimated PKN is smaller (see Table II and Fig. 3, first row). When all the PMJs are available, the resulting PKN (red tubes) can easily follow the branching pattern of the original underlying PKN (yellow tubes), with the estimated branches overlapping the original branches in most cases (distances between original and estimated PKN around 0 mm). In Fig. 3, it is highlighted using single headed arrows, the location of the estimated PKN branches that almost match between original ones. As expected, when estimated PMJs with Gaussian noise were used, LAT times changed and the corresponding estimated PKN started to diverge from the original PKN. This effect is clear in Fig. 3, where estimated branches are farther from the original than the same cases with less LAT error. The effect of the sample error is not linear with respect to the distance, as can be seen in Table II, since the morphology and complexity of the PKN also plays an important role.

When using the original PMJs ($\sigma = 0$) as input, Δ_{PMJs} (the difference in LAT at PMJs between original and obtained through the PKN) and Δ_{EAM} (errors after propagating the signal to all endocardial mesh points) are on average below 0.85 ms for all scenarios. The average distance between tree segments is smaller than 1 mm. In addition, around 95% of the PMJs could be connected to the tree with an error below $\epsilon_{max} < 4.0$ ms. Not all PMJs could be connected due to a restriction imposed on the PKN with respect to overlapping branches. It is noteworthy, that the number of PMJs in the model affected both errors Δ_{PMJs} and Δ_{EAM}. When models include a large density of PMJs (PK1, 1224 PMJs), Δ_{PMJs} and Δ_{EAM} where slightly smaller than for less crowded models (PK5, 206 PMJs).

When the estimated PMJs were used to build the PKN (see Fig. 3 second and third rows, and Table II), the CV_P in the PKN had to be estimated. Note that, for simplicity, in the simulations we used a reference CV_P of 1.0 m/s in the original PKN. In scenarios with estimated PMJs, the percentage of PMJs available to build the PKN decreased considerably. We used 1000 EAM samples to estimate the PMJs. In dense scenarios such as PK1 (1224 PMJs), we estimated 9.3% of PMJs when the Gaussian noise introduced was $\sigma = 0.5$, and 5.4% when $\sigma = 2.5$, while in coarser models such as PK5, we estimated 40.3% when the noise was $\sigma = 0.5$, and 27.7% when $\sigma = 2.5$. Since we only could estimate a subset of the original PMJs, the algorithm tends to overestimate the CV_P, as can be seen in Table II, where most cases have an optimal value above 1.0 m/s. Having less PMJs estimated, the resulting PKN is simpler (less branches), and the estimated CV is larger. In Table II the number of branches of each estimated PKN is summarized in column labeled '# Br'. Using the proposed methodology the number of branches in an estimated PKN is always the number of PMJs plus one branch (bundle branch).

Fig. 4 presents the activation maps of the original simulations, and those produced from the estimated PKNs for different errors, where it can be appreciated a very good match between the activation sequences. Errors at PMJs, Δ_{PMJs}, are below 1 ms in all scenarios, however, the average error across the mesh, Δ_{EAM}, (measured at the 1000 sampled EAM points)

TABLE II

ESTIMATION OF THE PKN FROM ESTIMATED PMJS. ESTIMATED CONDUCTION VELOCITIES (CV_P) ARE IN M/S. ϵ_{max} < THRESHOLD SHOWS THE PERCENTAGE OF ESTIMATED PMJS CONNECTED TO THE PKN BELOW A THRESHOLD ERROR. Δ_{PMJs} SHOWS THE AVERAGE TIME ERROR BETWEEN ESTIMATED TIME AT PMJS AND TIME AT WHICH THE WAVEFRONT ARRIVES THROUGH THE PKN. #BR SHOWS THE NUMBER OF BRANCHES IN THE PKN. Δ_{EAM} SHOWS THE AVERAGE TIME ERROR BETWEEN LAT AT ENDOCARDIAL SAMPLES AND TIME AT WHICH ACTIVATION WAVEFRONT ARRIVES USING THE ESTIMATED PKN

Name	σ	#PMJs	CV_P	ϵ <4ms	ϵ <1ms	Δ_{PMJs}	#Br	Distance error	Δ_{EAM}
PK1	0	1224	1	96.32%	84.23%	0.69 ± 0.6 ms	968	0.87 ± 1.32 mm	0.52 ± 0.3 ms
PK1	0.5	114	1.1	76.32%	62.28%	0.79 ± 0.9ms	86	2.20 ± 2.7mm	1.67 ± 1.8ms
PK1	2.5	67	1.2	50.75%	41.79%	0.96 ± 0.9ms	35	2.46 ± 3.1mm	4.48 ± 4.5ms
PK2	0	831	1	94.83%	79.42%	0.72 ± 0.6 ms	591	1.76 ± 2.61 mm	0.63 ± 0.5 ms
PK2	0.5	95	1.2	77.89%	60.00%	0.66 ± 0.7ms	74	2.11 ± 2.4mm	1.20 ± 1.4ms
PK2	2.5	66	1.2	63.64%	46.97%	0.88 ± 0.9ms	43	4.94 ± 5.1mm	3.24 ± 2.6ms
PK3	0	442	1	96.83%	88.20%	0.65 ± 0.6 ms	369	1.19 ± 1.39 mm	0.63 ± 0.5 ms
PK3	0.5	111	1.0	81.98%	63.96%	0.76 ± 0.8ms	90	1.92 ± 1.8mm	1.40 ± 1.4ms
PK3	2.5	68	1.3	69.12%	58.82%	0.72 ± 0.8ms	46	2.81 ± 1.3mm	2.70 ± 2.9ms
PK4	0	362	1	95.86%	78.45%	0.70 ± 0.6 ms	300	1.53 ± 1.58 mm	0.65 ± 0.5 ms
PK4	0.5	99	1.0	85.86%	69.70%	0.72 ± 0.6ms	86	2.17 ± 2.1mm	1.18 ± 1.2ms
PK4	2.5	68	1.1	75.00%	60.29%	0.71 ± 0.7ms	52	2.35 ± 2.0mm	2.54 ± 2.6ms
PK5	0	206	1	95.63%	80.58%	0.81 ± 0.7 ms	186	1.89 ± 2.06 mm	0.72 ± 0.8 ms
PK5	0.5	83	1.1	79.52%	57.83%	0.72 ± 0.5ms	67	3.09 ± 3.6mm	1.38 ± 1.6ms
PK5	2.5	57	1.3	78.95%	57.89%	0.83 ± 0.9ms	46	2.40 ± 2.2mm	2.37 ± 1.9ms

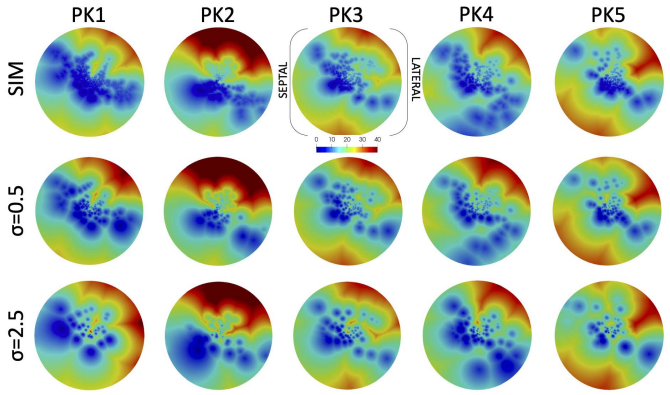

Fig. 4. Comparisons between LAT maps on synthetic models. Activation maps generated by original (SIM) and estimated PKNs subject to different Gaussian errors ($\sigma = 0.5$ and $\sigma = 2.5$), visualized on a projected disk. Times in the colorbar are provided in milliseconds.

increases due to two main reasons: i) the underestimation in the overall number of PMJs, which is around 10% of the real ones; and ii) the error in the LAT of the estimated PMJs. The same explanation applies to the increase in distance error, since due to the low number of PMJs and branches in the estimated PKN, the distance to the original PKN is larger. In summary, Δ_{EAM} is below 3 ms, even when $\sigma = 2.5$, in all scenarios except PK1, which has a very large number of PMJs.

B. Estimation of PKN From EAMs

The set of clinical EAMs acquired from patients was used to estimate the corresponding PKNs. First, all the EAMs were analyzed, filtered and re-annotated, obtaining more physiological patterns of activation (see Fig. 2). Table III, column '#Pts' indicates the final number of points available in each EAM after filtering, which was on average 195.

For the estimation of PMJs, an optimal CV for tissue (CV_T) has to be estimated for each case. Therefore, the estimation was carried out considering a range of CV_T between 0.4 m/s and 0.9 m/s, to take into account both potential slow propagation due to pathological tissue such as fibrosis, and fast conduction velocities due to underestimation of PMJs. For each CV_T, we obtained an estimation of the total number of PMJs, the number of EAM samples that support each of those PMJs (and their correlation), and the error Δ_{EAM} after propagating from the estimated PMJs to the endocardial samples. The best results were used as an input to estimate the PKN.

The number of PMJs obtained from the real cases ranged from 11 to 51, which was expected mainly due to the low number of endocardial samples finally used to estimate them (between 73 and 387 samples), the errors in the LAT maps and the sample location errors (a detailed geometry was not used in almost any case). The error Δ_{EAM} when directly activating the endocardium from the PMJs (PKN structure not considered) ranged from 3.61 ms to 20.20 ms, with an average of 8.13 ± 4.12 ms. This error can be explained looking at the percentage of EAM samples that were compatible with any of the PMJs estimated, which is included in Table III, column labeled as 'Link'. It is important to remark that during the estimation of the PMJs only a subset of the EAM samples actually produced PMJs for a given CV_T. i.e., the 'link' factor. In general, when less than 70% of the samples generate PMJs, LAT errors are large (> 10 ms). This is explained by the fact that, once the propagation from the PMJs is carried to the whole mesh, non-contributing EAM samples are not in agreement with the LATs, increasing the error. Therefore, the 'Link' is a measure of confidence in the PKN estimation, that can help assessing the accuracy together with the error Δ_{EAM}. There may be several reasons to explain small 'Link' numbers, such as wrongly annotated samples that make the map spatio-temporally incoherent, or tissue inhomogeneities that produce local changes in CV that affect the convergence of the inverse estimation. When considering only cases with a Link over 70%, the average error Δ_{PMJs} decreases to 6.10 ± 1.8 ms (Table III last row). To further validate the results, we performed a cross-validation in those cases where

TABLE III

QUANTITATIVE ANALYSIS OF ERRORS ON THE ESTIMATION OF THE PKN FROM CLINICAL EAMS. A/S STANDS FOR AGE/SEX; #PTS: POINTS OF EAM AFTER FILTERING; LINK: PERCENTAGE OF PTS CONSISTENT WITH ESTIMATED PMJS; CVS CONDUCTION VELOCITIES IN M/S FOR TISSUE (T) AND PURKINJE (P); TAT: TOTAL ACTIVATION TIME OF THE PMJS; #PMJS: ESTIMATED PMJS; ϵ_{max} < THRESHOLD, NUMBER OF ESTIMATED PMJS CONNECTED TO THE PKN BELOW A THRESHOLD ERROR; AVG: AVERAGE RESULTS; AVG> 70: AVERAGE FOR CASES WITH LINK OVER 70%

Patient			EAM		PMJ Estimation						PKN Estimation		
Study	A/S	Ind	Sampl	#Pts	Link	CV_T	CV_P	TAT	#PMJs	Δ_{EAM}	ϵ <5ms	Δ_{PMJs}	Δ_{EAM}
P1 LV			860	229	79%	0.5	1.7	56.7 ms	31	7.66 ms	30 (97%)	0.69 ± 0.7 ms	8.0 ms
P1 RV	50-M	HCM	810	276	69%	0.4	2.1	54.4 ms	34	15.96 ms	32 (94%)	1.30 ± 1.3 ms	16.0 ms
P2 LV			1460	230	85%	0.6	1.7	59.2 ms	37	5.70 ms	32 (86%)	0.73 ± 0.9 ms	7.2 ms
P2 RV	57-M	Lam	1523	371	88%	0.6	1.9	48.7 ms	38	6.65 ms	35 (92%)	0.70 ± 1.0 ms	6.9 ms
P3 LV			691	174	79%	0.8	1.7	38.0 ms	23	6.25 ms	20 (88%)	1.18 ± 1.4 ms	6.9 ms
P3 RV	34-M	IVF	744	165	92%	0.9	2.3	37.1 ms	16	4.76 ms	13 (81%)	0.79 ± 1.2 ms	5.2 ms
P4 LV			491	115	76%	0.8	1.7	57.6 ms	11	8.05 ms	9 (82%)	0.99 ± 1.3 ms	8.3 ms
P4 RV	58-M	IVF	539	161	76%	0.6	1.9	44.1 ms	19	11.02 ms	15 (79%)	0.63 ± 0.5 ms	13.6 ms
P5 LV			514	177	84%	0.9	1.7	28.0 ms	19	4.10 ms	18 (95%)	0.69 ± 0.6 ms	4.4 ms
P5 RV	18-M	IVF	532	190	93%	0.8	2.1	48.8 ms	20	5.60 ms	17 (85%)	0.67 ± 0.8 ms	5.8 ms
P6 LV			1224	191	76%	0.4	1.7	93.4 ms	28	8.34 ms	23 (82%)	0.93 ± 1.2 ms	9.5 ms
P6 RV	63-M	IVF	1494	313	63%	0.4	1.7	66.4 ms	39	20.20 ms	31 (79%)	0.68 ± 0.7 ms	21.0 ms
P7 LV			100	75	87%	0.8	2.1	36.48 ms	12	5.43 ms	12 (100%)	1.06 ± 1.5 ms	5.9 ms
P7 RV	16-M	IVF	189	115	64%	0.7	2.1	60.7 ms	17	10.90 ms	13 (76%)	1.06 ± 1.5 ms	12.1 ms
P8 LV			1044	284	89%	0.6	1.9	42.8 ms	38	5.63 ms	32 (84%)	1.00 ± 1.1 ms	6.1 ms
P8 RV	23-F	IVF	792	345	89%	0.6	2.5	44.4 ms	51	3.96 ms	47 (92%)	1.02 ± 1.0 ms	4.4 ms
P9 LV			874	320	86%	0.7	2.1	32.1 ms	39	3.91 ms	34 (87%)	1.06 ± 1.1 ms	4.5 ms
P9 RV	26-M	IVF	1064	387	91%	0.7	1.7	36.5 ms	43	3.61 ms	38 (88%)	0.87 ± 1.1 ms	4.7 ms
P10 LV			174	92	66%	0.8	1.7	24.2 ms	13	13.83 ms	11 (85%)	0.89 ± 1.0 ms	15.2 ms
P10 RV	51-M	IVF	169	78	88%	0.6	1.9	50.6 ms	13	7.56 ms	11 (85%)	0.68 ± 1.0 ms	9.4 ms
P11 LV			372	179	69%	0.4	1.9	91.7 ms	27	14.97 ms	25 (93%)	0.87 ± 1.1 ms	16.1 ms
P11 RV	41-M	BS	215	92	66%	0.7	1.9	80.9 ms	12	7.92 ms	10 (83%)	0.69 ± 0.6 ms	9.9 ms
P12 LV			315	219	72%	0.5	1.9	108.8 ms	37	6.42 ms	33 (89%)	0.25 ± 0.5 ms	6.7 ms
P12 RV	58-M	VT	78	73	81%	0.4	1.9	25.2 ms	17	5.29 ms	16 (94%)	0.39 ± 0.8 ms	5.5 ms
P13A LV			140	118	75%	0.9	2.3	20.5 ms	17	5.61 ms	16 (94%)	0.26 ± 0.3 ms	5.9 ms
P13A RV	53-M	VT	179	159	69%	0.6	2.3	32.4 ms	22	9.32 ms	19 (86%)	0.57 ± 1.0 ms	10.9 ms
P13B LV			198	151	72%	0.8	2.3	29.9 ms	21	6.39 ms	19 (90%)	0.36 ± 0.7 ms	6.4 ms
P13B RV	53-M	VT	188	177	62%	0.7	2.3	32.8 ms	14	12.51 ms	13 (93%)	0.33 ± 0.6 ms	13.2 ms
AVG	-	-		195	78%	0.7	1.96	47.8 ms	25	8.13 ms	22 (88%)	0.76 ± 0.9 ms	8.9 ms
AVG>70	-	-		203	83%	0.7	1.95	46.9 ms	27	6.10 ms	24 (89%)	0.75 ± 0.9 ms	6.8 ms

the Link value was high (around 80%). In particular, we estimated the PMJs from: i) 70% of the samples ($\#P_{stm}$), and left the remaining 30% ($\#P_{val}$) for validation of the LAT; and ii) using a leave-one-out cross validation. For the first case, we randomly selected the points to estimate and validate 20 times, and calculated the average values of all estimations, which are summarized in Table IV. As expected, in the first validation (70/30) # PMJs estimated decreased and the error $\Delta 70_{PMJs}$ increased around 2ms in average for each case. The leave-one-out cross validation obtained better results in error, $\Delta 1_{PMJs}$ (ms), since the PMJs were properly estimated and the increase in error was only due to non spatio-temporal coherent LATs. That means that the methodology requires denser EAMs and very accurate calculation of the annotated LATs to provide consistent results.

The CV in the PKN (CV_{PK}) also had to be estimated. The algorithm estimated PKNs for velocities in the range between 1.5 and 2.5 m/s on the best PMJ estimation solution, based on final average error Δ_{PMJs}. The final anatomy of the estimated PKN changes as a function of the CV_{PK}, since the sum of branch lengths has to shorten as we increase CV_{PK} for a given PMJ with a specific estimated LAT. For instamce, for a given set of estimated PMJs, using a $CV_{PK} = 1.7$ m/s, branches in the septum branch out earlier (shorted path from AV node to PMJ is required) than the case of $CV_{PK} = 2.3$ m/s. The arrival time at the PMJs also changes, and therefore the LAT of the PMJs differs (within the allowed threshold), resulting in different errors and number of PMJs connected. For most of the cases, summarized in Table III, the optimal CV_{PK} was between 1.7 m/s and 2.1 m/s, with an average of 1.95 m/s, which resulted in more than 80% of PMJs connected and average errors Δ_{PMJs} under 1.3 ms (Table III, column 'Δ_{PMJs}'). Δ_{PMJs} is the difference between the estimated PMJ activation time and the time when the PMJ is activated through the estimated PKN.

For the PKN estimation, the maximum error allowed at a PMJ to connect a branch to it was set to $\epsilon_{max} < 5$ ms, to keep average errors under a reasonable threshold. The number of estimated PMJs connected to the PKNs was on average 88%. Since in most scenarios estimated PMJs included PMJs incorrectly estimated, we expected that the PKN algorithm filtered some of them, and therefore a 100% connection was not desirable. In fact, when more PMJs were connected to a PKN the average LAT error Δ_{PMJs} increased, which required a trade-off between PMJs connected and average LAT error. We chose to get the maximum number of PMJs connected, with a maximum average LAT error Δ_{PMJs} below 1.3 ms. As can be observed in Table III, Δ_{PMJs} was on average 0.76 ± 0.9 ms.

Fig. 5 summarizes a comparison of LV LAT maps for ten patients, including the re-annotated EAMs used to estimate the PKN (first row), the PMJs estimated and the LAT map

TABLE IV
CROSS-VALIDATION OF THE ESTIMATION OF PMJS FOR A SET OF REPRESENTATIVE DATASETS. $\#P_{stm}$ IS THE NUMBER OF SAMPLES USED TO ESTIMATE PMJS, AND $\#P_{val}$ THE NUMBER OF SAMPLES USED TO VALIDATE THEM USING A 70/30 CROSS-VALIDATION. CROSS-VALIDATION ERRORS FOR 70/30, $\Delta 70_{PMJs}$, AND FOR LEAVE-ONE-OUT, $\Delta 1_{PMJs}$, IN MS

Name	$\#P_{stm}$	$\#P_{val}$	#PMJs	$\Delta 70_{PMJs}$	$\Delta 1_{PMJs}$
PK2 LV	161	69	30.5	7.88	7.41
PK2 RV	259	112	30.5	8.63	8.08
PK3 LV	121	53	20.3	8.02	7.73
PK3 RV	115	50	10.0	6.15	5.72
PK5 LV	124	53	18.8	6.40	4.93
PK5 RV	133	57	17.7	6.90	6.67
PK8 LV	199	85	34.1	8.39	6.76
PK8 RV	241	104	43.1	7.24	5.67
PK9 LV	224	96	34.2	6.74	5.11
PK9 RV	271	116	37.0	5.27	4.41
PK12 LV	153	66	23.4	8.89	7.81
PK12 RV	53	22	9.30	14.41	13.03

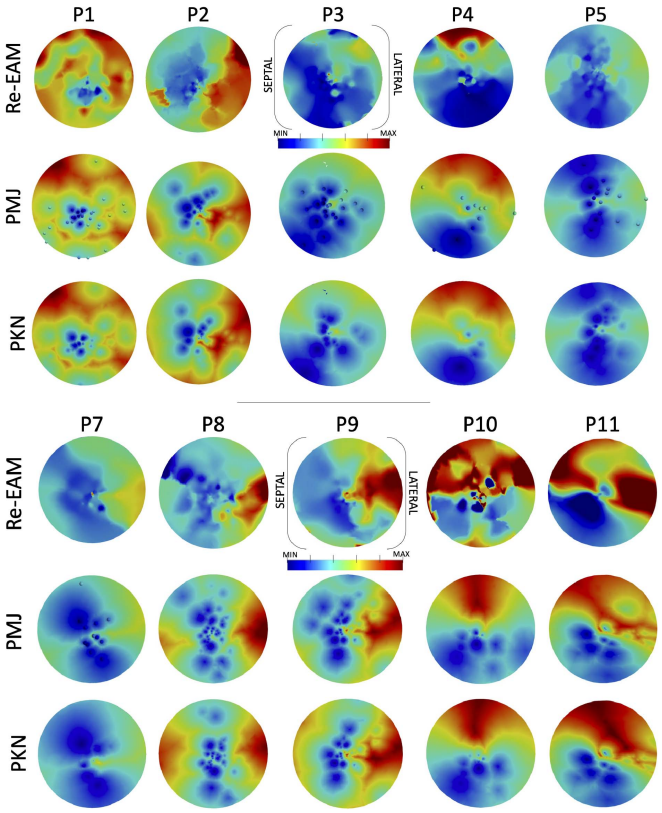

Fig. 5. Comparisons between projected LV LAT maps for five patients, showing i) EAM re-annotated and interpolated (first row), ii) Simulated LAT map from estimated PMJs (no PKN included, stimulated from tissue) (second row), and iii) Simulated LAT map from estimated PKN (third row). Maps are color-coded from $t = 0$ ms (blue regions) to $t = max$ ms (red regions), relative to each EAM.

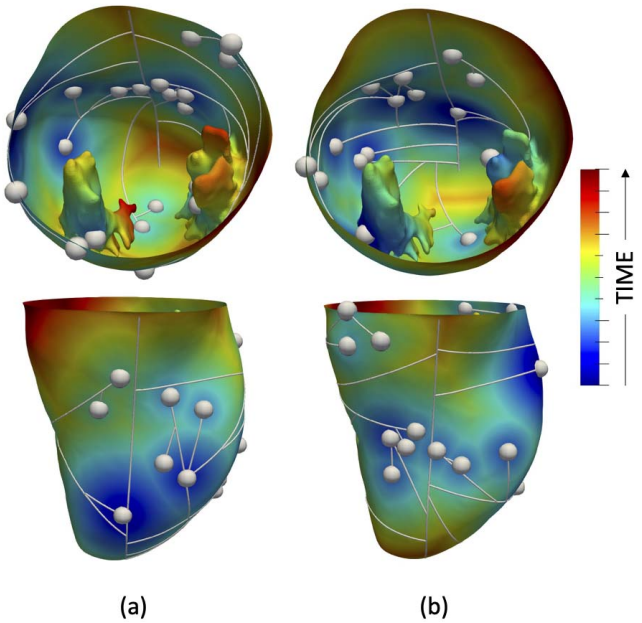

Fig. 6. Comparison of PKNs estimated from two different EAM studies from the same patient. LATs (first row) and Error at PMJs (second row) for (a) study 1 (P13A), and (b) study 2 (P13B).

obtained when simulating from the PMJs (second row), and the LAT map obtained when the activation was triggered from the estimated PKN (third row). As can be observed, the PMJ and PKN LAT maps are very similar, since most PMJs were connected to the corresponding PKN and the LAT errors Δ_{PMJs} were small (see Table III, column 'Δ_{PMJs}'). However, there are differences with respect to the EAM, specially for the case of patients P1 and P2. EAM maps shown in the first row are obtained after re-annotating the LAT of the endocardial samples and interpolating the data. Therefore, it is important to take into account that the resulting interpolated LAT map is not exactly the real activation sequence of the patient, since the activation time range is bounded by the earliest and latest sample acquired. Moreover, a Gaussian kernel is used to interpolate the LATs, which introduces a smoothing effect that reduces the range of the LATs. Overall, the best results were obtained for P5 LV, P8 RV, and P9 (see Table III, column 'Δ_{EAMs}'). The reason for those improved results was a larger number of EAM samples (above 300 in most of them) together with a high Link factor ($> 84\%$). On the contrary, the worst cases showed Link values around 63% and large errors. The number of PMJs estimated did not correlate with the error, although the best cases included more than 30 PMJs estimated, which is above the average (22 PMJs) in our study. There was an outlier, patient P6, that showed an error Δ_{EAMs} of 21.0 ms, which was really high compared with the other cases. This particular case corresponded to a case with NICD (QRSd 138 ms), which probably had some problems at the level of the PKN, or the myocardial tissue, which hamper the estimation that assumes homogeneous CV on both media during the optimization procedure. Only a very dense and curated EAM could provide enough information to estimate local non-homogeneous CVs in a reliable way.

For the particular case of patient P12, the LATs annotated for each point in the EAM were manually corrected by an expert electrophysiologist, and inconsistent samples were removed. In addition, the endocardial anatomy was obtained from MRI, and the EAM was mapped to it. As a result, we observed that a larger proportion of PMJs could

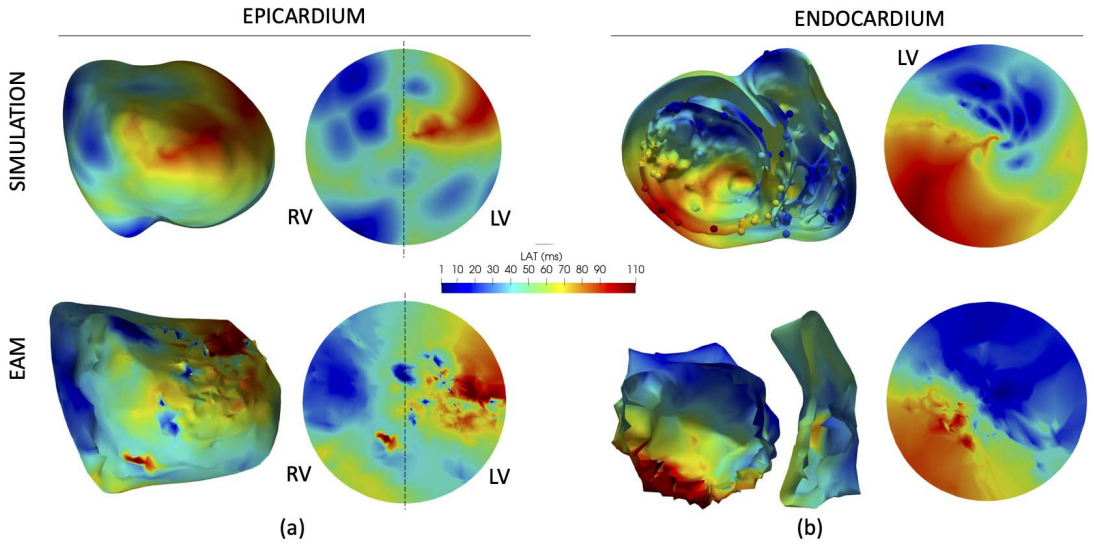

Fig. 7. Comparison between simulated LAT and EAM for P12. LATs obtained by simulating patient P12 using the estimated PKN (top row), compared to LATs from patient EAM (bottom row). (a) Epicardial LATs on the 3D mesh (left) and equivalent projected onto a disk (right). (b) Endocardial LATs on the 3D mesh and projection of the LV onto a disk.

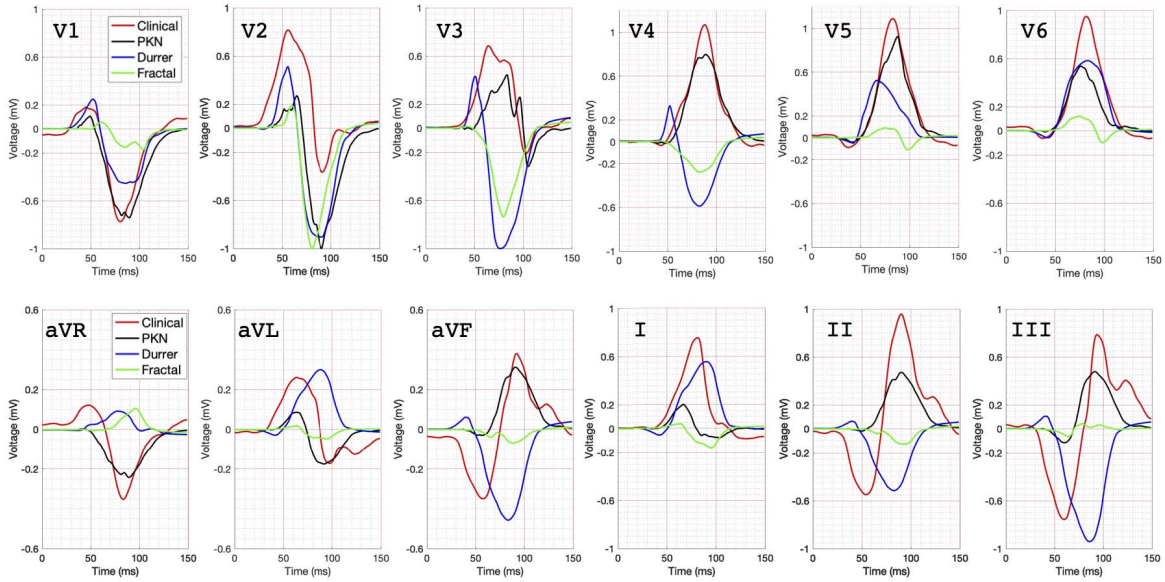

Fig. 8. Comparison between clinical and simulated 12-lead ECG on patient P12 geometry. Each subplot includes, the clinical patient ECG recorded at precordial leads in sinus rhythm (red traces), the Simulated ECG using the estimated PKN (black traces), the simulated ECG using discrete endocardial points to match Durrer's [20] activation sequence (blue traces), and the simulated ECG using an stochastic PKN generated using L-systems [7] (green traces).

be estimated, compared to other cases with more samples. In addition, both the number of PMJs connected and the average errors were smaller. For patient P13, we had two different EAM studies (P13A and P13B), which were used to obtain two different estimations of the PMJ set. As can be observed in Table III and Fig. 6, the optimal CVs (2.3 m/s) in the PKN matched for both ventricles in both cases. The estimated PMJs for each study differs in the number of PMJs (e.g. LV (a) 17 vs (b) 21) and the location of some of them. When the PKN was estimated, the final number of PMJs was almost the same (LV (a) 16 vs (b) 19), and the sequence of activation showed a similar pattern with respect to early and late activated regions. Nonetheless, we did not observe a perfect coincidence between the LAT maps since the original EAMs were not identical, despite being recorded from the same patient. We performed a cross-validation between both EAMs, i.e., estimating the PMJs from one EAM and validating the activation sequence with the second. As expected, the errors were large: i) Estimating with PK13A and validating with PK13B, we obtained an error of 9.9ms and 19.1ms for LV and RV, respectively. That fact reveals that since EAMs: i) show only partial and interpolated information to electrophysiologist, and ii) assume stationarity on the electrical activation over time, two different acquisitions might show maps that do not match. Therefore, estimated

PKN can only aim at reproducing the EAM data observed and not the location of PMJs, provided that enough samples have been acquired. Note that although the results activating from the PMJs are better that using the PKN, it is necessary to include the PKN structure since in many pathological scenarios involving arrhythmias the PKN is activated retrogradely from the tissue, which completely changes the normal order of activation of PMJs.

To further validate the PKN method, we performed full biventricular biophysical simulations for patients P3, P5, P8, P9, and P12 using the corresponding estimated PKNs, and the geometry of P12 as reference, where all EAMs were fit. All the details about the protocol to perform the biophysical simulations can be found in [19]. As can be observed in Fig. 7 for P12, the EAM activation sequences in the epicardium (a) and the endocardium (b), were properly reproduced by the simulation, following the main patterns. The total activation times of the EAM and the simulation matched each other. We also simulated the electrical activation obtained in the 3D model using commonly used approaches, namely the sequence of activation that mimicked Durrer's descriptions [20], and the one resulting from a fractal-based generic Purkinje system generated using L-systems as in [7].

The extracellular potentials generated in the heart for each configuration were propagated to the torso surface to obtain the 12-lead ECG. Fig. 8 shows for each lead the clinical ECG recorded from the patient (red trace), together with three tested configurations: estimated PKN (black traces), Durrer's activation (blue traces), and stochastic PKN generated using L-systems (green traces). From the plots it can be appreciated that PKN configuration (black trace), i.e. the estimated PKN, reproduces the polarity of the signal in all precordial leads V1-V6. In V3 and V4, the other configurations (Durrer and Fractal) show negative polarity, as compared with the clinical and PKN ECGs. The worst case was obtained for lead V2, which could be due to the displacement of the patient's lead due to the location of a CARTO patch necessary for the EAM system. The extended leads also provided a good match in terms of polarity for the PKN configuration, although signal amplitudes differed in most cases. This was expected due to the fact that our torso model does not have limps, and in addition the organ conductivities were not optimized for this particular patient, and instead generic values from the literature were used. For the rest of the simulations we compared the clinical and the simulated 12-lead ECGs, as depicted in Fig. 9, and obtained a very close match in terms of QRS duration, polarity and in most cases amplitude. Finally, we compared quantitatively the ECGs by calculating the Pearson's correlation between the clinical ECG and the simulated one using the estimated PKNs. Table V shows the results. As displayed in bold face, the P12 PKN configuration outperforms all the other generic activation sequences used in the modeling literature, showing the highest correlation (>0.80) for all leads, except lead V6 (correlation) and lead I (RMSE) in which Durrer's configuration showed better results. For the rest of estimated PKNs (fit to P12 geometry), the correlation was very high except for three particular cases: P5-V3, P8-V3 or P9-V6. These results highlight the importance of the activation sequence of the endocardium compared to other factors such as the patient-specific cardiac geometry.

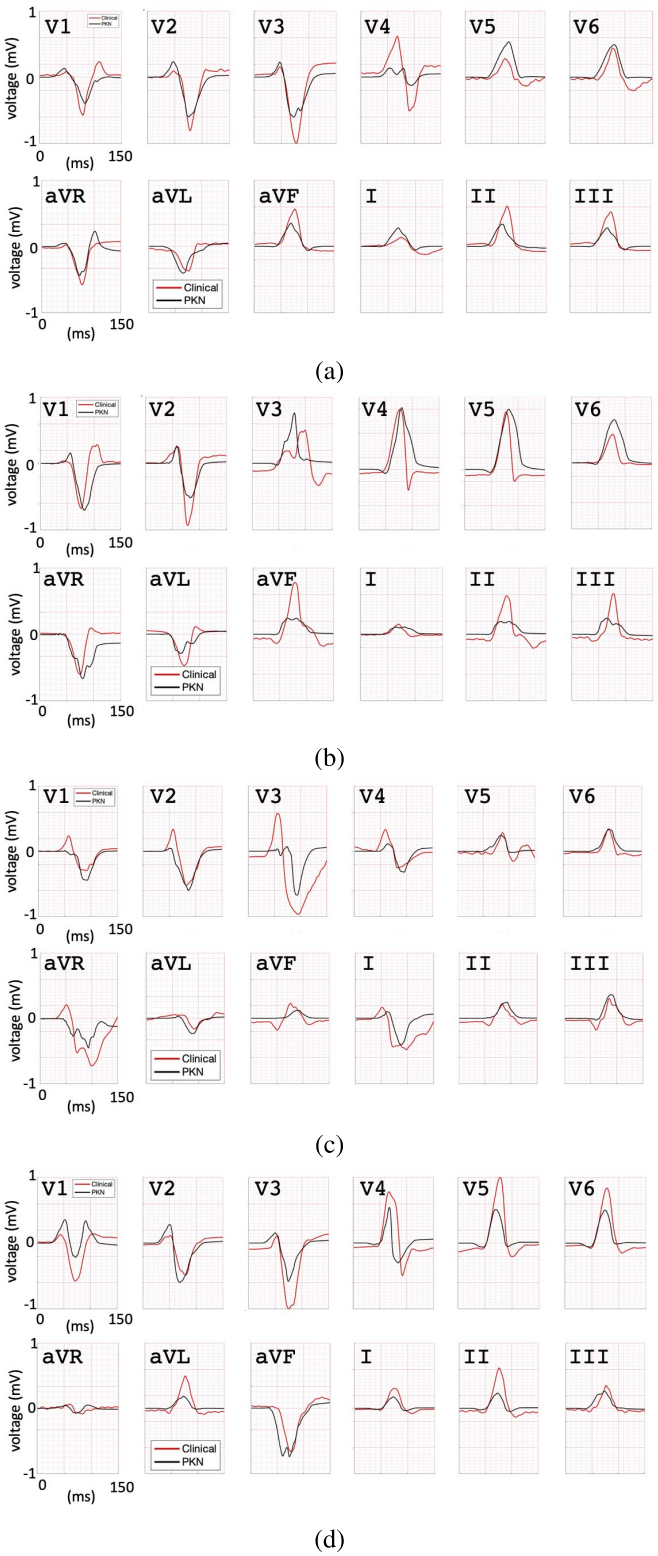

Fig. 9. Comparison of clinical and simulated 12-lead ECGs using estimated PKNs. Red plots correspond to clinical traces, and black plots to simulated ones, for (a) P3, (b) P5, (c) P8, and (d) P9.

TABLE V
QUALITY INDICES OF SIMULATED 12-LEAD ECGS FOR THREE DIFFERENT ACTIVATION CONFIGURATIONS

Model	V1	V2	V3	V4	V5	V6	aVR	aVL	aVF	I	II	III
P3	0.77	0.93	0.92	0.84	0.90	0.92	0.86	0.95	0.92	0.84	0.93	0.82
P5	0.58	0.95	0.37	0.69	0.73	0.87	0.89	0.81	0.86	0.71	0.88	0.69
P8	0.78	0.93	0.61	0.80	0.93	0.94	0.68	0.96	0.76	0.81	0.78	0.79
P9	0.87	0.92	0.96	0.96	0.98	0.30	0.95	0.99	0.95	0.97	0.97	0.96
P12	**0.95**	**0.62**	**0.83**	**0.97**	**0.82**	0.94	**0.53**	**0.92**	**0.81**	0.41	**0.87**	**0.72**
Durrer	0.94	0.49	-0.51	-0.91	0.78	**0.96**	0.22	-0.68	-0.33	**0.78**	-0.56	-0.13
Fractal	0.75	0.24	-0.67	-0.97	0.31	0.47	0.22	-0.79	-0.46	-0.48	-0.73	0.69

IV. DISCUSSION

In this work, we have presented a novel methodology to estimate a PKN for a given patient by estimating its PMJs and branching structure from an EAM. From the estimated model, it is possible to obtain information about the PMJ locations (early activated regions) as well as reproduce the patient electrical sequence of activation and the ECG using computer simulations. This is important since the Purkinje system has been shown to play a crucial role in several types of cardiac arrhythmia, such as VT or idiopathic VF [11]. The PKN cannot be directly observed in vivo and it is very complex to map with current clinical technology [5]. This is one of the main reasons why having accurate computer models of the PKN to carry out biophysical simulations is so important. Clinically, a better knowledge of the PKN structure of a patient showing VT triggered from the PKN could help in the identification of ablation sites. Recently, it has been proposed the use of ablation for "De-Networking" of the Purkinje system in cases in which it has been implicated as a source of initiation of VF [21].

In the modeling literature the most common approach to build a PKN is manually [22], [23], by developing random networks based on fractals (L-systems), or following optimization criteria [3], [24], [25]. Some authors have chosen to segment the proximal sections of the PKN in animals such as dog [6] using Lugol's solution or calf [7] using Indian ink. Many computational studies simply neglect the PKN and focus on pathologies, where there is little involvement of the ventricular conduction system, such as scar-related VT [26], [27]. Having a more faithful PKN, able to reproduce the sequence of activation of a specific patient with an error of a few milliseconds, can help in virtual therapy planning and optimization of RFA or cardiac resynchronyzation therapy (CRT) [22].

A. PKNs From Synthetic Models

By means of a simulation study, we have verified that the methodology presented is able to estimate the most relevant PMJs or early activated areas with small spatio-temporal errors. In addition, the main bundles of the PKN (anterior and posterior) could be properly reconstructed, and most of the estimated PMJs ($> 80\%$) successfully connected to the PKN considering physiological CVs in both tissue and PKN. The percentage of estimated PMJs that can be successfully connected to the PKN decreases as we increase σ from 0.5 to 2.5, due to errors in location and LAT of estimated PMJs (note that Gaussian noise was inserted in the samples as described in [14]). In general, the percentage of estimated PMJs that are connected to the PKN with $\epsilon_{max} < 4$ ms is around 75%. In distal areas, where the branching pattern is complex, the morphology could not be reproduced, but only simplified representations of the PKN. It is important to remark that since branch intersections are not allowed by design, the resulting PKN is a tree instead of a closed network. Nonetheless, the estimated PKN can reproduce the sequence of activation observed in the EAM of the patient, avoiding the use of a random PKN with an arbitrary number of PMJs. Errors at PMJs, Δ_{PMJs}, were below 1 ms in all scenarios.

B. PKNs From Patient EAMs

A few computational studies have also focused on the in vivo estimation of a compatible PKN from EAMs [10], [28], [29]. For instance, in [28], a complex fractal-based PKN is built on the endocardium as a background network, and following PMJs are either moved, removed or added to the network to reduce the error Δ_{EAM}. Our minimal PKNs, estimated from the data, had less than 100 branches and 50 PMJs (see Table III), while the fractal models in [28] had between 1500 and 2500 branches, and 200 to 250 PMJs, similar to our synthetic PKNs. Still, there is a remarkable difference in the optimal CV_{PK} obtained in our study that ranged between 1.7 and 2.1 m/s, compared to the 3.9 m/s obtained in [28], or 2.25 m/s used in [6]. It is important to point out that the average conduction velocity of 1.95 m/s estimated in the PKN was very stable between cases, and can be considered as a physiological parameter for the human PKN. Although conduction velocities for PKN in the range of 3-4 m/s [20] have been used in several computational studies, some experimental studies have reported other data: 1.85 m/s [30], 2.2 m/s [31], 1.56 $\pm$ 0.59 m/s [32], 1.41 $\pm$ 0.4 m/s [33], and 1.62m/s [34].

We avoided performing a CV over-fitting, that is, adapting locally the CV in different regions so that our simulation match exactly the clinical data. Instead, we opted for a global optimization of the CV within physiological ranges, which is what would be expected in a real helathy PKN.

One of the main advantages of the method proposed is that the PKN is built from estimating the optimal branches for the estimated PMJs, while other methods use simple criteria to place the PMJs [10]. In such approach, one could place the PMJs exactly on each of the endocardial EAM samples, and

use the measured LAT, obtaining an error Δ_{EAMs} of 0 ms. However, that will not correspond to any possible PKN for a patient, since EAM samples do not correspond to PMJs. In our approach, each of the PMJs that is placed in our model can explain the activation of many endocardial EAM samples, i.e. it is compatible with their spatio-temporal location given a global CV.

It is important to point out that sparse EAMs or wrongly annotated ones will cause a reduction in the number of estimated PMJs, which in turn could generate poor PKNs with larger errors in the activation maps. In this study, after filtering the patient EAMs, the number of endocardial samples was always under 400 points, which makes it difficult to obtain a large number of estimated PMJs. Four of the PKN models, namely P8 and P9 (LV and RV), which showed smaller errors, correspond to high density EAMs. That is why it is key to use high-dense maps such as those provided by multi-polar catheters. However, we did not observe a direct relationship between the number of PMJs estimated for a given model and the final error at the EAM samples. One of the most relevant measures of quality is the Link percentage. Therefore, estimated PKNs with a 'Link' factor (percentage of EAM samples that gave rise to PMJs) under 70% should be considered carefully or discarded, since the PKN will not be able to reproduce the sequence of activation in at least 30% of the samples. This generates, on average, errors above 10 ms, which cannot be considered a personalized activation. We encountered this problem in 8 out of 28 PKN models estimated. Those studies will require a careful revision of EAM LATs, and analysis of local inhomogeneities.

Other studies have reported mean absolute errors at the endocardial mesh, using an estimated PKN, between 4.9 ± 4.1 ms and 7.4 ± 6.6 ms [28], and 5.8 ± 4.5 ms in [9], but using EAMs provided by EnSite NavX system, and patient geometry segmented from MRI. Errors obtained in our models fitted to a segmented LV endocardium were 6.42 ms (219 EAM samples) for patient P12, and 5.61 ms (118 EAM samples), and 6.39 ms (151 EAM samples) for the two maps of P13. Including all cases, if we consider PKNs with Link higher than 70% (Table III, AVG$>$ 70), the average error at EAM from the PKN was 6.10 ± 1.8 ms.

Finally, we showed by means of biophysical simulations that the sequence of activation generated by the personalized PKN from five patients produced as a result virtual ECGs comparable in morphology to the patient clinical ones, and showed a high correlation ($>$ 80%) in almost all 12-leads ECG. In addition, virtual ECGs generated by stochastic procedures or following descriptions from the literature resulted in non-physiological ECGs. To our knowledge, other studies that try to estimate the PKN have never obtained the corresponding ECGs by simulation. Although, previous studies on synthetic PKN such as [25], [35] obtained simulated ECGs to compare the effect of model parameters or simulate His-Bundle pacing in different scenarios [36]. It is important to remark that comparing simulated and clinical ECG can be only considered as a surrogate validation.

There are several limitations of the methodology. First of all, the estimated PKNs are trees, and not networks with closed loops, as observed in real Purkinje networks at both proximal [4], [5] and terminal sections [37]. That feature provides the network with resiliency in case of local conduction blocks, or damage of part of the tissue, but since we cannot estimate the location of those loops, we choose not to add them synthetically. However, if desired, loops could be created in the required density, without altering the LATs at the PMJs. The location of the estimated PMJs depends indirectly on the location of the endocardial samples acquired in the cathlab, and therefore, non-homogeneous maps will give rise to unbalanced PMJ distributions and PKN morphologies. A homogeneous sampling is therefore required to obtain meaningful PKNs that can be compared among patients. It is important to remark that we could not validate the morphology of the PKN, or the location of the estimated PMJs in real patients, since all the studies are performed in vivo. However, the results obtained in synthetic PKN showed that the estimated PKNs were similar to the original ones (comparing distance and angles), and the location of estimated PMJs was close to original one. Nonetheless, to obtain accurate results, the number of endocardial samples, and their LAT error should be bounded. Finally, we observed that in patients with pathologies that affect conduction velocities, such as patient P6 (NICD), the error Δ_{EAMs} increases with respect to other cases. That inhomogenous activation which might affect the PKN should be specially treated, and probably consider several CVs on the PKN to account on local delays.

In conclusion, we believe that incorporating more personalized information to the biophysical models of the heart, or even into the EAM systems, could help in therapy planning and optimization. The use of computer models to optimized therapies require not only the personalization of the anatomy of the heart but also their electrical properties. In that sense, having a more personalized PKN model and sequence of activation that help to understand patient particularities or enable to study the effect of different treatments on the ECG would be fundamental. In this paper, we aimed at estimating and validating the methodology in patients that are in sinus rhythm. In the future, we will analyze whether the presented methodology is useful to predict potential arrhythmia mechanisms sustained by the Purkinje system, and planning RFA ablation targeted at the Purkinje system. In such scenario, it would be important to record the location from which electrophysiologist trigger the arrhythmia in the patient and the resulting ECG, so that it can be reproduced in silico to validate the retrograde activation sequence of the PKN.

On the other hand, if the estimation method developed would be integrated into an EAM navigation system, the mapping could be guided, improving the robustness of the results.

REFERENCES

[1] M. E. Silverman, D. Grove, and C. B. Upshaw, "Why does the heart beat? The discovery of the electrical system of the heart," *Circulation*, vol. 113, no. 23, pp. 2775–2781, Jun. 2006.

[2] A. J. Atkinson *et al.*, "Functional, anatomical, and molecular investigation of the cardiac conduction system and arrhythmogenic atrioventricular ring tissue in the rat heart," *J. Amer. Heart Assoc.*, vol. 2, no. 6, Nov. 2013.

[3] E. J. Vigmond and B. D. Stuyvers, "Modeling our understanding of the His–Purkinje system," *Prog Biophys Mol Biol*, vol. 120, nos. 1–3, pp. 179–188, Jan. 2016.

[4] A. J. Atkinson, S. R. Kharche, M. G. Bateman, P. A. Iaizzo, and H. Dobrzynski, "3D anatomical reconstruction of human cardiac conduction system and simulation of bundle branch block after TAVI procedure," in *Proc. 38th Annu. Int. Conf. IEEE Eng. Med. Biol. Soc. (EMBC)*, Aug. 2016, pp. 5583–5586.

[5] R. S. Stephenson *et al.*, "High resolution 3-Dimensional imaging of the human cardiac conduction system from microanatomy to mathematical modeling," *Sci. Rep.*, vol. 7, no. 1, p. 7188, Aug. 2017.

[6] E. M. Cherry and F. H. Fenton, "Contribution of the purkinje network to wave propagation in the canine ventricle: Insights from a combined electrophysiological-anatomical model," *Nonlinear Dyn.*, vol. 68, no. 3, pp. 365–379, May 2012.

[7] R. Sebastian, V. Zimmerman, D. Romero, D. Sanchez-Quintana, and A. F. Frangi, "Characterization and modeling of the peripheral cardiac conduction system," *IEEE Trans. Med. Imag.*, vol. 32, no. 1, pp. 45–55, Jan. 2013.

[8] S. Ryu, S. Yamamoto, C. R. Andersen, K. Nakazawa, F. Miyake, and T. N. James, "Intramural Purkinje cell network of sheep ventricles as the terminal pathway of conduction system," *Anatomical Rec.*, vol. 292, no. 1, pp. 12–22, Jan. 2009, doi: 10.1002/ar.20827.

[9] S. Palamara, C. Vergara, E. Faggiano, and F. Nobile, "An effective algorithm for the generation of patient-specific purkinje networks in computational electrocardiology," *J. Comput. Phys.*, vol. 283, pp. 495–517, Feb. 2015.

[10] R. Cárdenes, R. Sebastian, D. Soto-Iglesias, A. Berruezo, and O. Camara, "Estimation of purkinje trees from electro-anatomical mapping of the left ventricle using minimal cost geodesics," *Med. Image Anal.*, vol. 24, no. 1, pp. 52–62, Aug. 2015.

[11] M. Haissaguerre, E. Vigmond, B. Stuyvers, M. Hocini, and O. Bernus, "Ventricular arrhythmias and the His–Purkinje system," *Nature Rev. Cardiol.*, vol. 13, no. 3, pp. 155–166, Mar. 2016.

[12] A. Nogami, "Purkinje-related arrhythmias Part I: Monomorphic ventricular tachycardias," *Pacing Clin. Electrophysiol.*, vol. 34, no. 5, pp. 624–650, May 2011.

[13] M. Haissaguerre, G. Cheniti, W. Escande, A. Zhao, M. Hocini, and O. Bernus, "Idiopathic ventricular fibrillation with repetitive activity inducible within the distal purkinje system," *Heart Rhythm*, vol. 16, no. 8, pp. 1268–1272, Aug. 2019.

[14] F. Barber, I. García-Fernández, M. Lozano, and R. Sebastian, "Automatic estimation of purkinje-myocardial junction hot-spots from noisy endocardial samples: A simulation study," *Int. J. Numer. Methods Biomed. Eng.*, vol. 34, no. 7, p. e2988, Jul. 2018.

[15] D. Soto Iglesias *et al.*, "Quantitative analysis of electro-anatomical maps: Application to an experimental model of left bundle branch block/cardiac resynchronization therapy," *IEEE J. Transl. Eng. Health Med.*, vol. 5, Jan. 2017, Art. no. 1900215.

[16] M.-H. Yueh, W.-W. Lin, C.-T. Wu, and S.-T. Yau, "An efficient energy minimization for conformal parameterizations," *J. Sci. Comput.*, vol. 73, no. 1, pp. 203–227, Oct. 2017.

[17] M. J. Bishop *et al.*, "Development of an anatomically detailed MRI-derived rabbit ventricular model and assessment of its impact on simulations of electrophysiological function," *Amer. J. Physiol.-Heart Circulatory Physiol.*, vol. 298, no. 2, pp. H699–H718, Feb. 2010.

[18] R. Doste *et al.*, "A rule-based method to model myocardial fiber orientation in cardiac biventricular geometries with outflow tracts," *Int. J. Numer. Methods Biomed. Eng.*, vol. 35, no. 4, p. e3185, Apr. 2019.

[19] A. Lopez-Perez, R. Sebastian, M. Izquierdo, R. Ruiz, M. Bishop, and J. M. Ferrero, "Personalized cardiac computational models: From clinical data to simulation of infarct-related ventricular tachycardia," *Frontiers Physiol.*, vol. 10, p. 580, May 2019.

[20] D. Durrer, R. T. Van Dam, G. E. Freud, M. J. Janse, F. L. Meijler, and R. C. Arzbaecher, "Total excitation of the isolated human heart," *Circulation*, vol. 41, no. 6, pp. 899–912, Jun. 1970.

[21] G. Imnadze and T. Zerm, "Prevention of ventricular fibrillation through de-networking of the Purkinje system: Proof-of-concept paper on the substrate modification of the Purkinje network," *Pacing Clin. Electrophysiol.*, vol. 42, no. 10, pp. 1285–1290, Oct. 2019.

[22] D. Romero *et al.*, "Effects of the Purkinje system and cardiac geometry on biventricular pacing: A model study," *Ann. Biomed. Eng.*, vol. 38, no. 4, pp. 1388–1398, Apr. 2010.

[23] E. J. Vigmond and C. Clements, "Construction of a computer model to investigate sawtooth effects in the Purkinje system," *IEEE Trans. Biomed. Eng.*, vol. 54, no. 3, pp. 389–399, Mar. 2007.

[24] E. Behradfar, A. Nygren, and E. J. Vigmond, "The role of Purkinje-myocardial coupling during ventricular arrhythmia: A modeling study," *PLoS ONE*, vol. 9, no. 2, Feb. 2014, Art. no. e88000.

[25] F. Sahli Costabal, D. E. Hurtado, and E. Kuhl, "Generating Purkinje networks in the human heart," *J. Biomech.*, vol. 49, no. 12, pp. 2455–2465, Aug. 2016.

[26] N. A. Trayanova and K. C. Chang, "How computer simulations of the human heart can improve anti-arrhythmia therapy," *J. Physiol.*, vol. 594, no. 9, pp. 2483–2502, May 2016.

[27] D. Deng, A. Prakosa, J. Shade, P. Nikolov, and N. A. Trayanova, "Sensitivity of ablation targets prediction to electrophysiological parameter variability in image-based computational models of ventricular tachycardia in post-infarction patients," *Frontiers Physiol.*, vol. 10, p. 628, May 2019.

[28] C. Vergara *et al.*, "Patient-specific generation of the Purkinje network driven by clinical measurements of a normal propagation," *Med. Biol. Eng. Comput.*, vol. 52, no. 10, pp. 813–826, Oct. 2014.

[29] S. Palamara *et al.*, "Computational generation of the Purkinje network driven by clinical measurements: The case of pathological propagations," *Int. J. Numer. Methods Biomed. Eng.*, vol. 30, no. 12, pp. 1558–1577, Dec. 2014.

[30] R. W. Joyner and E. D. Overholt, "Effects of octanol on canine subendocardial Purkinje-to-ventricular transmission," *Amer. J. Physiol.-Heart Circulatory Physiol.*, vol. 249, no. 6, pp. H1228–H1231, Dec. 1985.

[31] A. Maguy *et al.*, "Ion channel subunit expression changes in cardiac Purkinje fibers: A potential role in conduction abnormalities associated with congestive heart failure," *Circulat. Res.*, vol. 104, no. 9, pp. 1113–1122, May 2009.

[32] M. R. Rosen, M. J. Legato, and R. M. Weiss, "Developmental changes in impulse conduction in the canine heart," *Amer. J. Physiol.-Heart Circulatory Physiol.*, vol. 240, no. 4, pp. H546–H554, Apr. 1981.

[33] K. T. Cragun, S. B. Johnson, and D. L. Packer, "β-adrenergic augmentation of flecainide-induced conduction slowing in canine Purkinje fibers," *Circulation*, vol. 96, no. 8, pp. 2701–2708, Oct. 1997.

[34] R. J. Myerburg, H. Gelband, K. Nilsson, A. Castellanos, A. R. Morales, and L. A. Bassett, "The role of canine superficial ventricular muscle fibers in endocardial impulse distribution," *Circulat. Res.*, vol. 42, no. 1, pp. 27–35, Jan. 1978.

[35] L. Dux-Santoy, R. Sebastian, J. Felix-Rodriguez, J. M. Ferrero, and J. Saiz, "Interaction of specialized cardiac conduction system with antiarrhythmic drugs: A simulation study," *IEEE Trans. Biomed. Eng.*, vol. 58, no. 12, pp. 3475–3478, Dec. 2011.

[36] J.-I. Okada *et al.*, "Longitudinal dissociation and transition in thickness of the His–Purkinje system cause various QRS waveforms of surface ECG under His bundle pacing: A simulation study based on clinical observations," *J. Cardiovascular Electrophysiol.*, vol. 30, no. 11, pp. 2582–2590, Nov. 2019.

[37] D. Romero, O. Camara, F. Sachse, and R. Sebastian, "Analysis of microstructure of the cardiac conduction system based on three-dimensional confocal microscopy," *PLoS ONE*, vol. 11, no. 10, 2016, Art. no. e0164093.